Characterization of Electronic Transport through Amorphous TiO_2 Produced by Atomic-Layer Deposition

Paul Nunez,[†] Matthias H. Richter, [†] Christopher W. Roske, [†] Miguel Cabán-Acevedo, [†] Brandon D. Piercy, [‡] Mark D. Losego, [‡] Steven J. Konezny, [§,□] David J. Fermin, [⊥] Shu Hu,[*, §,#] Bruce S. Brunschwig, [▽] and Nathan S. Lewis*[,†, ▽,±]

[†] Division of Chemistry and Chemical Engineering, California Institute of Technology, Pasadena, California 91125, USA.

[‡] School of Materials Science and Engineering, Georgia Institute of Technology, Atlanta GA 30332, USA.

[§] Energy Sciences Institute, Yale West Campus, West Haven, CT 06516, USA.

[□] Department of Chemistry, Yale University, 225 Prospect Street, P.O. Box 208107, New Haven, Connecticut, 06520-8107, USA.

[⊥] School of Chemistry, University of Bristol, Cantock's Close, Bristol BS8 1TS, United Kingdom.

[#] Department of Chemical and Environmental Engineering, School of Engineering and Applied Sciences, Yale University, New Haven, CT 06520, USA.

[▽] Beckman Institute and Molecular Materials Research Center, California Institute of Technology, Pasadena, CA 91125, USA.

[±] Kavli Nanoscience Institute, California Institute of Technology, Pasadena, California 91125, USA.

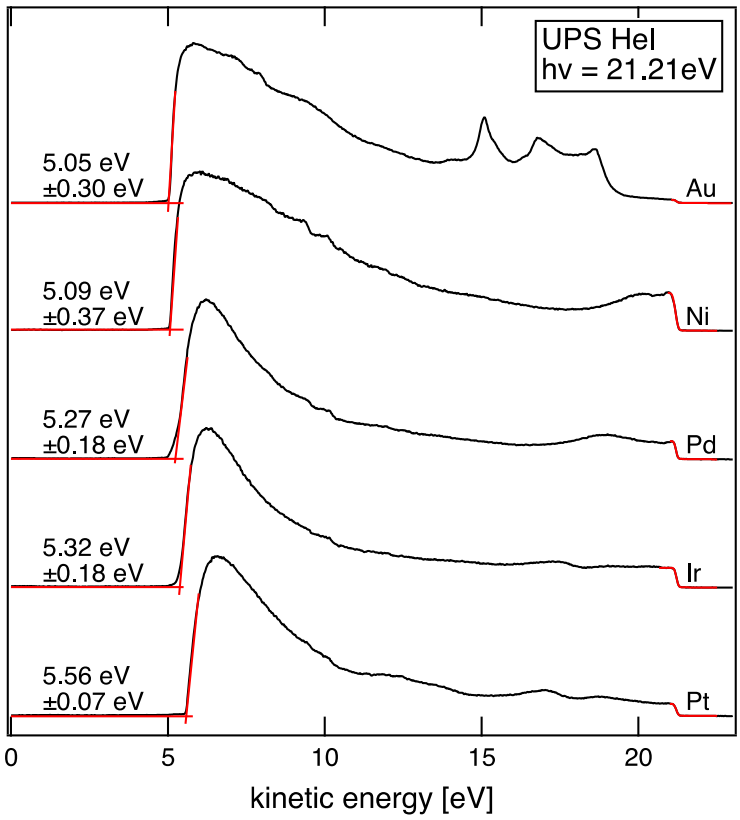

Figure S1 Ultraviolet photoelectron spectra for Ni, Pd, Pt, Ir, and Au. The work function for each element is indicated. The intersections of the two red lines on the low and high kinetic energy sides indicate the positions of energy of the secondary electron cutoff and the Fermi energy, respectively.

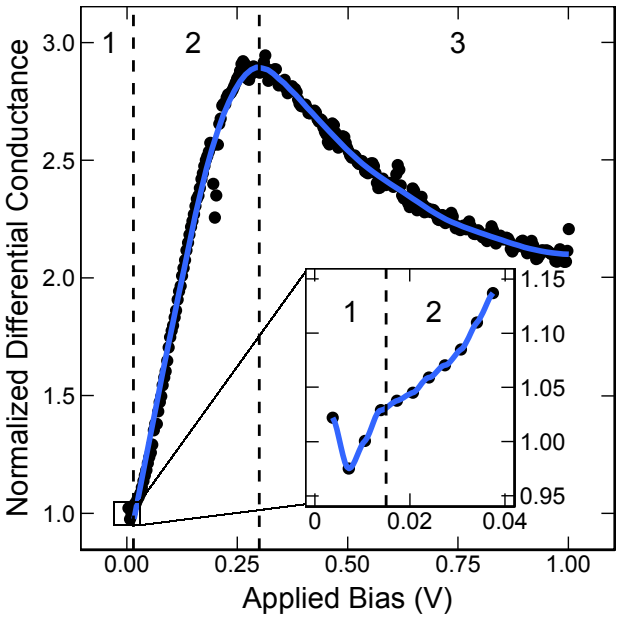

Figure S2 Normalized differential conductance for a p^+-Si|*a*-TiO_2|Ni device and *J-V* data plotted to show specific regions. The ohmic regime (region I) is depicted in a) and b), with the Schottky regime (region II) as well as the Fowler-Nordheim (like) transport (region III) depicted in c) and d). The normalized differential conductance is defined as $\frac{dJ}{dV}\left(\frac{V}{J}\right)$.

Table S1. Contact resistance measured by transmission line measurement method for various metal contacts. The compensated voltage was using the current respectively listed to the left.

Top Contact	Contact Resistance (Ω)	Current @ 10^{-2} V (A)	Compensated Voltage (V)	Current @ 0.1 V (A)	Compensated Voltage (V)
Ti	945 ± 44	~8×10^{-6}	7.6×10^{-3}	~100×10^{-6}	9.5×10^{-2}
Ir	5450 ± 750	~1×10^{-6}	5.5×10^{-3}	~10×10^{-6}	5.5×10^{-2}

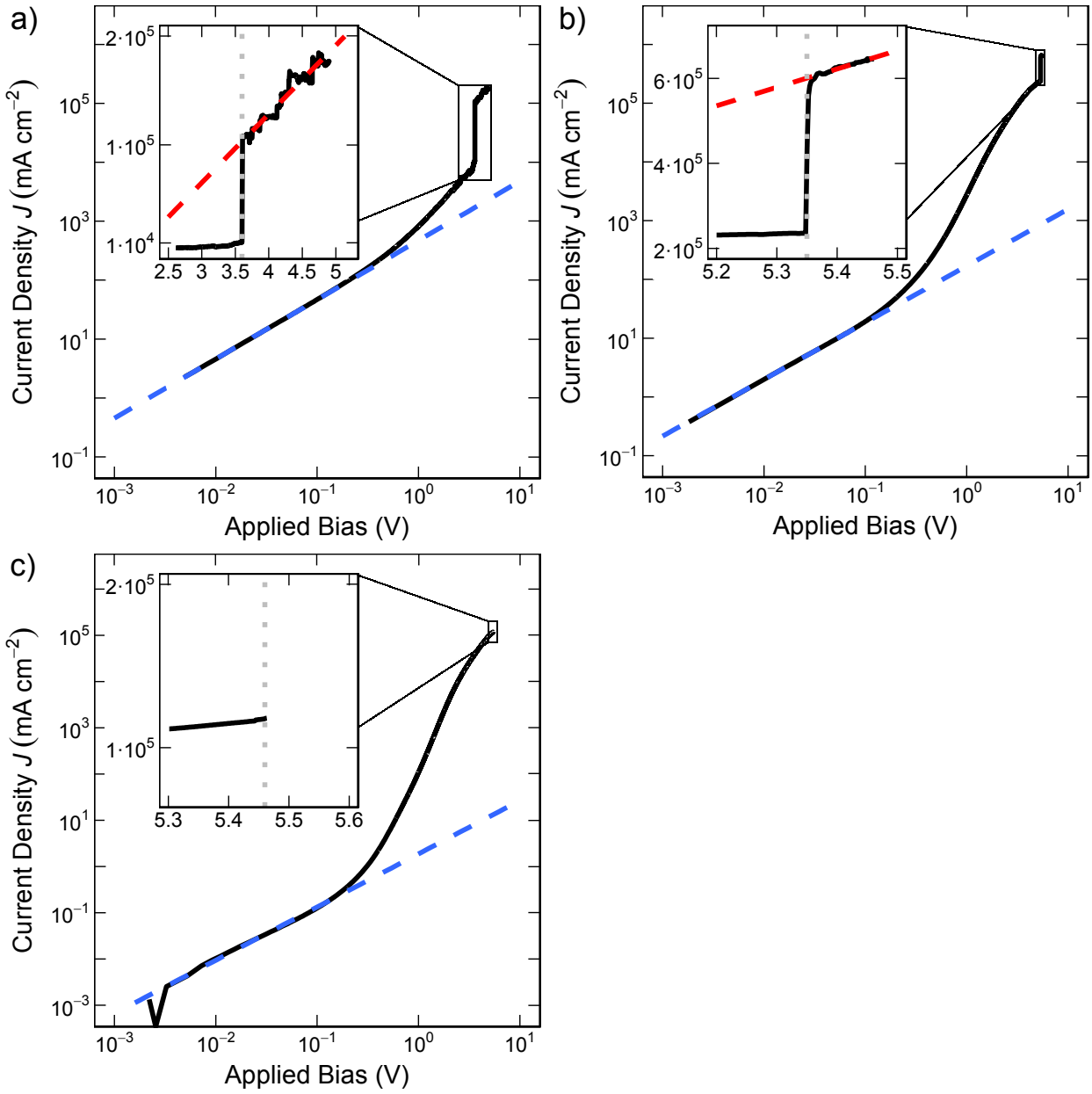

Figure S3 - *J-V* characteristics of a solid-state (a) p^+-Si|*a*-TiO_2|Au, (b) p^+-Si|*a*-TiO_2|Ir and (c) p^+-Si|*a*-TiO_2|Pd device, extended to applied biases > 5 V. The *a*-TiO_2 was ~ 68 nm thick. The inset is a plot of the crossover into the trap-filled regime. Linear regressions are shown for the ohmic region at low bias (blue dashed line), and the trap-filled space-charge-limited regimes (red dashed line in the inset). All devices had a secondary region except the p^+-Si|*a*-TiO_2|Pd device which exceeded the current limit of the potentiostat.

Table S2. Calculated trap densities, mobilities, and effective mobile charge-carrier densities for p^+-Si|*a*-TiO_2|metal devices with various metal top contacts.

	Trap Density (cm^{-3})	Mobility ($cm^2\ V^{-1}\ s^{-1}$)	Effective Mobile Charge-carrier Density (cm^{-3})
Mg	N/A	N/A	$(1.64\pm1.0)\times10^{16}$
Ti	N/A	N/A	$(2.54\pm1.2)\times10^{16}$
Ni	N/A	N/A	$(2.88\pm1.5)\times10^{16}$
Au	$(1.40\pm0.17)\times10^{19}$	$(2.08\pm0.02)\times10^{-4}$	$(3.83\pm2.4)\times10^{15}$
Ir	$(9.65\pm0.32)\times10^{18}$	$(9.45\pm0.26)\times10^{-4}$	$(2.66\pm1.3)\times10^{15}$
Pd	$(1.14\pm0.081)\times10^{19}$	N/A	$(6.38\pm3.29)\times10^{14}$
Pt	$(9.36\pm0.26)\times10^{18}$	$(5.67\pm0.15)\times10^{-4}$	$(6.35\pm4)\times10^{14}$

The interdigitated electrodes (IDEs) were used to measure the potential resolved conductance (EC-FET) in the *a*-TiO_2 (Figure 5). The conductance, *G,* was obtained from the conductivity by use of the cell constant, ($\sigma_{ecfet} = K \cdot G_{ecfet}$) where *K* is the cell constant and was estimated from:

$$K = \frac{2}{l(n-1)}\left(\frac{s}{w}\right)^{1/3} \quad \text{(S1)}$$

where *s* is the spacing between the electrode digits, *w* is the width of the electrode, *l* is the length, and *n* is the number of digits, 20 µm, 20 µm, 0.2 cm and 224, respectively. This relationship produced a cell constant of $K = 0.045$ cm^{-1}. Samples showed a weak potential dependence of the conductance (G_{ecfet}) in the potential range -0.25 to 1.75 V vs RHE.

Table S3. Conductance and conductivity for the corresponding IDE samples.

Sample	G_{ecfet} / S	σ_{ecfet} / S cm^{-1}
1	2.2×10^{-4}	9.8×10^{-6}
3	3.8×10^{-4}	1.7×10^{-5}
4	1.9×10^{-4}	8.6×10^{-6}

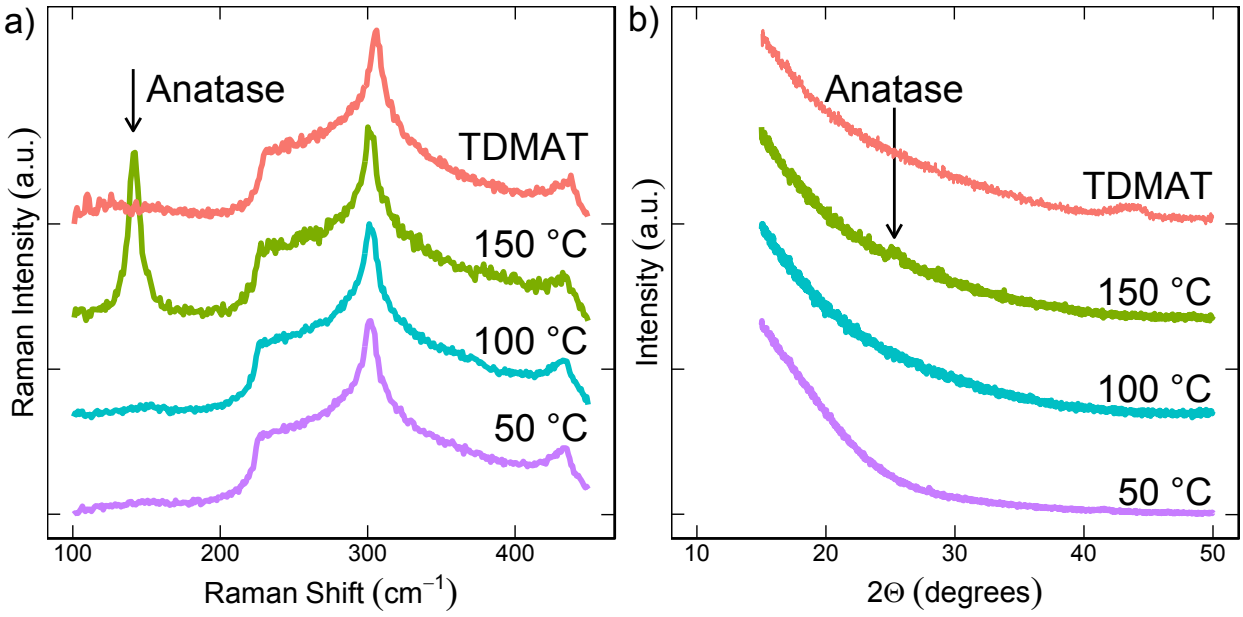

Figure S4 – a) Raman measurement of the various ALD deposited $TiCl_4$ precursor TiO_2 films and the same films measured by b) glancing incident x-ray diffraction (GIXRD). $TiCl_4$ films deposited at 50 and 100 ºC as well as the TDMAT film had an undetectable amount of crystallinity as evident in the lack of signal in the appropriate region of the Raman and GIXRD measurements. The film deposited at 150 ºC had a small fraction of crystallinity (Anatase) from the regions marked in both the Raman and GIXRD measurements.

Figure S5.a,b shows the ATR-IR spectra for ALD TiO_2 films deposited using glass and silicon as the substrates, and $TiCl_4$ and TDMAT as the titanium precursor. On the ATR-IR spectra we observed that main peak features can be assigned to IR absorptions coming from the substrate. Furthermore, we observed the absence of Ti-OH absorption peaks related to metatitanic acid (H_2TiO_3) within the IR region of 3310 cm^{-1} and 1200–1071 cm^{-1}, indicating that the ALD TiO_2 films deposited in this work are free of H_2TiO_3 species.[1]

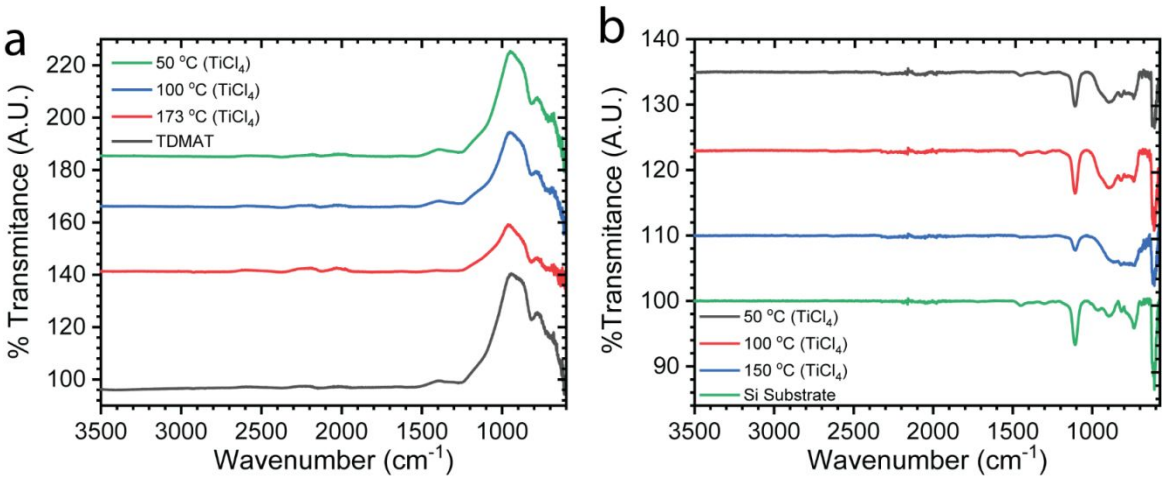

Figure S5 – ATR-IR spectra for ALD TiO2 films on a) glass and b) silicon substrate.

The charge transfer across the Ti|a-TiO_2|Ti|Ir|electrolyte junction can be modeled in terms of a double barrier generating a potential drop across the metal-insulator-catalyst (V_{Ω}) and catalyst-electrolyte junctions (V_{tafel}),[2-4]

$$V_{total} = \mathrm{V}_{\Omega} + V_{Tafel} = \frac{L}{q\mu N_D} i + \alpha \times 2.303 \ln\left(\frac{i}{i_0}\right) \quad \text{(S2)}$$

where L, α and i_0 are the a-TiO_2 film thickness, Tafel slope and the exchange current density, respectively. We assumed that the current is kinetically controlled across the potential range.

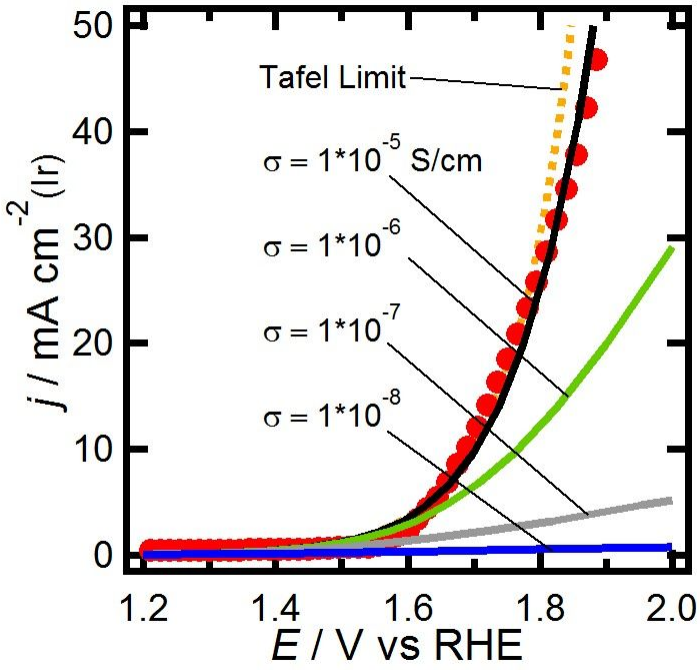

Figure S6. Comparison of the current-voltage curve obtained for p^+-Si|a-TiO_2|Ti|Ir films in 1 M H_2SO_4 with the values obtained from eq. S2, taking $\alpha = 41$ mV dec^{-1} and $I_0 = 0.07$ mA cm^{-2} . It should be noted that the current has been renormalized with respect to the area covered by the Ir islands (14% coverage), since charge transfer is negligible in the absence of the catalysts. The orange trace shows the Tafel limit (charge transfer unhindered by the TiO_2 layer), which is very close to the experimental values though somewhat lower than on state-of-the-art Ir catalysts.[5-6] The simulations show that a-TiO_2 conductivity of the order of 10^{-5} S cm^{-1} has very little influence on the voltammetric responses, while significant current damping can be observed upon decreasing the conductivity by one order of magnitude. These trends demonstrate that the characteristic conductivity measured for the a-TiO_2 film obtained by ALD are capable of sustaining current in the range of 10 mA cm^{-2} without the need of invoking mediation by the valence or conduction bands.

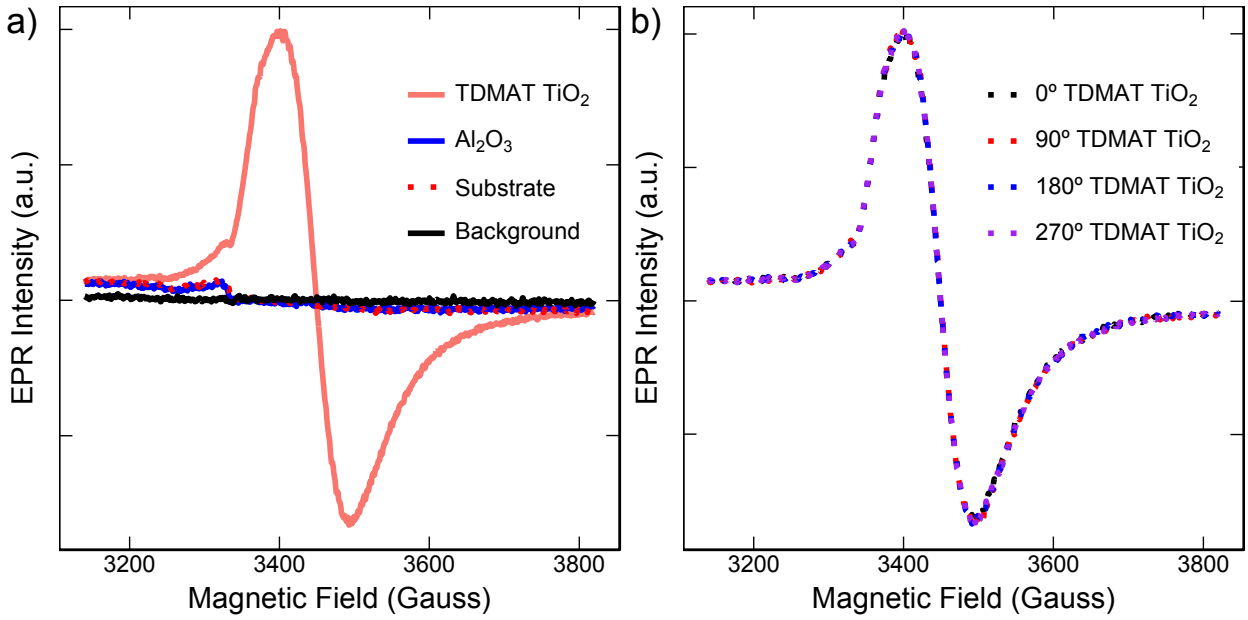

Figure S7. a) Comparison of the EPR spectra of TDMAT TiO_2 to the EPR spectra of ALD-deposited Al_2O_3, substrate-only and the background (an empty EPR tube). The broad peak was only present in the TDMAT TiO_2 whereas the slight bend at ~3300 G was due to the substrate. b) Comparison EPR spectra of TDMAT *a*-TiO_2 at various angles of rotation. The signal was independent of any rotation that the sample had with respect to the magnetic field.

Table S4. Attenuation length d for valence band states depending on excitation energy and take off angle Θ. λ was calculated with QUASES-IMFP-TPP2M.

	d for Θ=0°	d for Θ=70°
AlKa (1486.6eV)	28.23 Å	9.66 Å

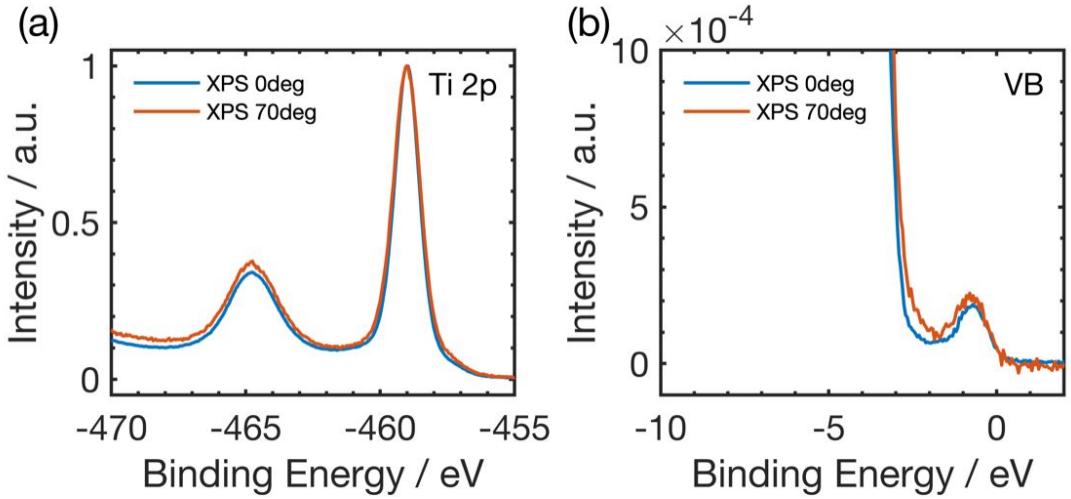

Figure S8. XPS spectra of the Ti 2p core levels and of the valence band for different emission angles (Θ=0° and 70°) relative to the surface normal. With increased surface sensitive (increased Θ), an increase in the oxygen shoulder at 532.5 eV was observed.[7]

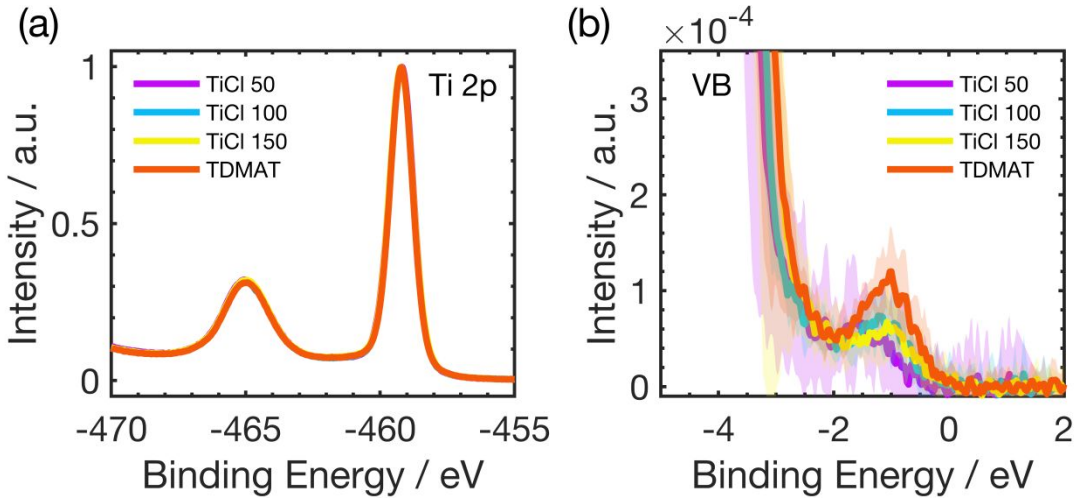

Figure S9. Average XPS (a) Ti 2p and (b) valence band spectra for TDMAT, $TiCl_4$-150, $TiCl_4$-100 and TiCl4-50 ºC for 10 different sample for each species. The average spectra and respective standard deviation has been calculated for the valence band spectra and is visible in (b).

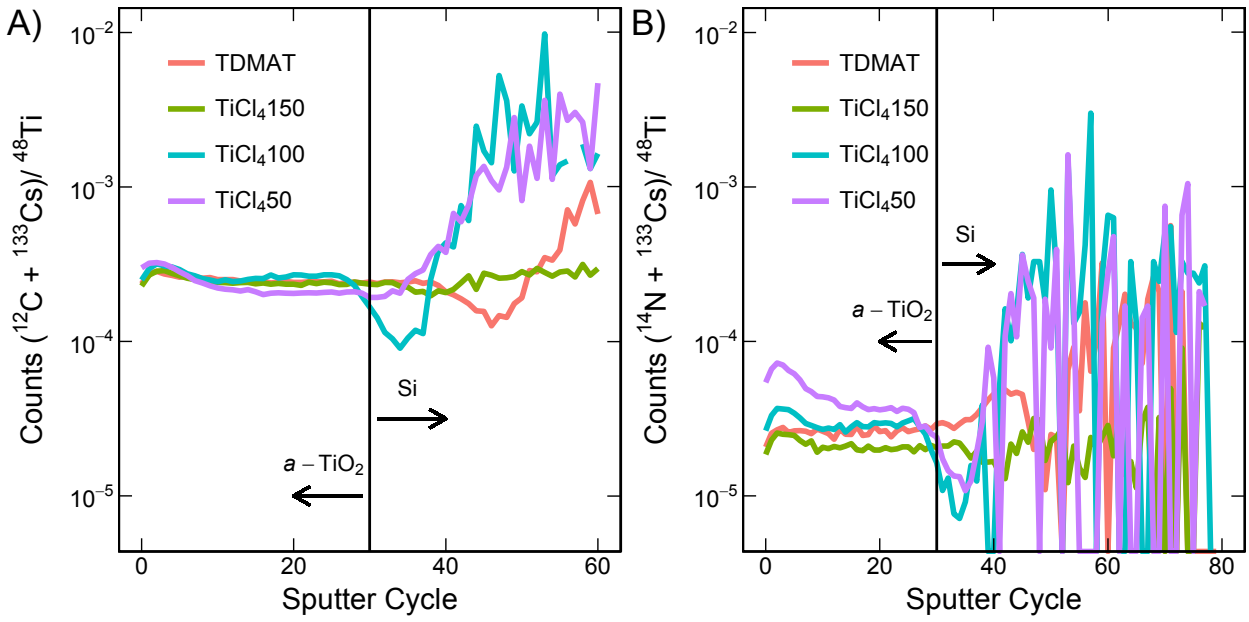

Figure S10. Normalized SIMS spectra of (a) ^{12}C and (b) ^{14}N for all *a*-TiO_2 samples. The first 30 sputter cycles are measuring the *a*-TiO_2 while the remaining cycles are measuring the underlying p^+-Si substrate. When comparing the SIMS spectra with the respective conductivity, no trend is apparent.

References

1. Mockūnaitė, S.; Ostachavičiūtė, S.; Valatka, E., Photocatalytic and Adsorptive Properties of Titanium Dioxide Prepared by Thermal Decomposition of Metatitanic Acid. *Chemija* **2012**, *23*.
2. Chazalviel, J.-N.; Allongue, P., On the Origin of the Efficient Nanoparticle Mediated Electron Transfer across a Self-Assembled Monolayer. *J. Am. Chem. Soc.* **2011**, *133*, 762-764.
3. Kissling, G. P.; Miles, D. O.; Fermín, D. J., Electrochemical Charge Transfer Mediated by Metal Nanoparticles and Quantum Dots. *Phys. Chem. Chem. Phys.* **2011**, *13*, 21175-21185.
4. Bradbury, C. R.; Zhao, J.; Fermín, D. J., Distance-Independent Charge-Transfer Resistance at Gold Electrodes Modified by Thiol Monolayers and Metal Nanoparticles. *J. Phys. Chem. C* **2008**, *112*, 10153-10160.
5. Reier, T.; Oezaslan, M.; Strasser, P., Electrocatalytic Oxygen Evolution Reaction (Oer) on Ru, Ir, and Pt Catalysts: A Comparative Study of Nanoparticles and Bulk Materials. *ACS Catal.* **2012**, *2*, 1765-1772.
6. McCrory, C. C. L.; Jung, S.; Ferrer, I. M.; Chatman, S. M.; Peters, J. C.; Jaramillo, T. F., Benchmarking Hydrogen Evolving Reaction and Oxygen Evolving Reaction Electrocatalysts for Solar Water Splitting Devices. *J. Am. Chem. Soc.* **2015**, *137*, 4347-4357.
7. Lichterman, M. F., et al., Direct Observation of the Energetics at a Semiconductor/Liquid Junction by Operando X-Ray Photoelectron Spectroscopy. *Energy Environ. Sci.* **2015**, *8*, 2409-2416.